Chemical Engineering Journal 534 (2026) 175078

Contents lists available at ScienceDirect

Chemical Engineering Journal

journal homepage: www.elsevier.com/locate/cej

Non-contact mechanical stimulation sensing and high-voltage direct current conversion system utilizing liquid metals

Tao Lin [a,b,1], Jiangtao Guo [a,1], Qingju Liu [a,c], Zhigang Chen [b], Yong Zhang [d], Wen Yang [e], Jun Wang [e], Peizhi Yang [a,*], Liangfei Duan [e,*]

[a] School of Energy and Environment Science, Southwest United Graduate School, Yunnan Normal University, Kunming, Yunnan, 650092, China
[b] Yunnan Vocational Institute of Energy Technology, Qujing, 655000, China
[c] Yunnan Key Laboratory for Micro/Nano Materials & Technology, School of Materials and Energy, Yunnan University, Kunming, 650091, China
[d] Department of Electrical and Computer Engineering, The University of North Carolina at Charlotte, Charlotte, NC, 28223, USA
[e] College of Chemistry and Chemical Engineering, Yunnan Normal University, Kunming, 650500, China

ARTICLE INFO

Keywords:
Liquid metals
Non-contact energy harvesting
Electromechanical conversion
Force-electric coupling
High voltage direct current

ABSTRACT

The non-contact energy harvesting technologies are critical for microelectronic devices, especially in special scenarios such as enclosed spaces or extreme environments. Room-temperature liquid metals (LM), possessing both metallic and fluidic elastic properties, have emerged as the preferred materials for high-density integration, morphological reconfigurability, high performance stability, and stringent biocompatibility standards. Herein, we present a flexible ultrasonic energy harvesting and direct current (DC) generation system based on LM. This system relies on an interface between eutectic gallium-indium-tin alloy (eGaInSn) LM and silicon dioxide in the system. The device leverages the inherent properties of LM, utilizing electromechanical coupling technologies to facilitate intelligent perception, collection, and transformation of non-contact ultrasonic energy stimulation. This innovative approach culminates in a high-voltage DC output and facilitates dynamic DC power amplification without rectification circuits. The device outputs a notable voltage of up to 2.5 kV under a load in a double electrode configuration, while a single electrode design attains an exceptional open-circuit voltage (V_{oc}) as high as 6 kV. This work expands the basic understanding of LM, electromechanical conversion, and force-electric coupling, leading to straightforward practices for ultrasonic energy harvesting and high-performance DC output. It also offers promising potential for future self-powered sensing systems, human-computer interfaces, arrayed broadcast group high-efficiency charging, and wearable energy solutions.

1. Introduction

Efficient ambient energy harvesting is crucial for powering the rapidly expanding network of Internet of Things (IoT) devices, especially for self-sustained systems [1]. Among various energy sources, mechanical energy is widely available as a dispersed environmental byproduct and shows great potential. Acoustic waves, which carry mechanical energy, offer inherent advantages for energy harvesting: they propagate through solid, liquid, and gas media and enable non-contact transmission [2]. However, the use of audible sound is limited by its random frequency and low energy density, leading to energy dissipation [3]. In contrast, ultrasound (typically >20 kHz) provides a coherent, high-energy alternative. It allows focused energy delivery with high spatial resolution and penetrability, making it ideal for efficient mechanical energy harvesting [4].

Ultrasonic energy harvesting, a cornerstone of self-powered microsystems, is anchored in three paradigms—piezoelectric, electromagnetic, and triboelectric mechanisms—each with entrenched limitations [5]. Piezoelectric converters, reliant on brittle ceramics (e.g., $PbZnTiO_3$, $BaTiO_3$) or semi-flexible polymers (e.g., Poly(vinylidene fluoride) (PVDF)) [6], deliver high energy density but falter in fatigue resistance and conformal integration, their intrinsic stiffness incompatible with dynamic microenvironments [7]. Although electromagnetic generators are robust and durable, their application in the ultrasonic frequency band is still limited by biocompatibility and structural complexity [8]. Triboelectric nanogenerators (TENGs) have emerged as versatile

* Corresponding authors.
E-mail addresses: pzhyang@hotmail.com (P. Yang), liangfeiduan1012@163.com (L. Duan).
[1] Tao Lin and Jiangtao Guo contributed equally to this work.

https://doi.org/10.1016/j.cej.2026.175078
Received 29 July 2025; Received in revised form 22 February 2026; Accepted 8 March 2026
Available online 10 March 2026
1385-8947/© 2026 Elsevier B.V. All rights are reserved, including those for text and data mining, AI training, and similar technologies.

alternatives [9], yet conventional solid-state designs—employing Polytetrafluoroethylene (PTFE), or metallic interfaces—remain tethered to contact-separation cycles [10]. This contact dependency exacerbates material wear, accelerates degradation, and induces parasitic damping, critical flaws in high-frequency, non-contact ultrasonic scenarios [11]. Compounding these issues, all three mechanisms produce alternating current (AC), necessitating inverter rectification circuits that introduce energy loss, system complexity, and barriers to miniaturization.

Recent advances in TENGs focus on multifunctional integration and output enhancement, yet most remain confined to contact-driven mechanisms. Representative systems include Liu et al.'s layered smart fabrics (self-cleaning/thermal management, contact-separation-dependent [12]), Xia et al.'s reported metal-free water cup TENG (liquid-solid contact, low-voltage AC [13]) and all-foam sensor (contact-reliant pressure detection [14]), as well as the alloy powder-based Faraday cage-inspired TENG (ocean sensing, contact-based [15]) and double-piezoelectric-layer-enhanced designs (efficiency improved, contact limitations unaddressed [16]). All share a fundamental constraint: solid-phase materials and direct contact/liquid-solid interactions induce interface wear, limit stability and dynamic coupling, and restrict applications to contact-accessible scenarios.

In contrast, we introduce a paradigm shift using LM' spontaneous polarization and dynamic charge transport at solid-liquid-gas triple-phase interfaces. Breaking dual constraints of solid-phase materials and contact-driven mechanisms, this design enables the first stable direct current output under non-contact mechanical excitation via an elastomer-like interface—eliminating wear and expanding non-contact applicability to open new pathways for soft energy harvesting.

LM, by virtue of their exceptional fluidity and high electrical conductivity [7,17,18], exhibit remarkable advantages in making conformal contacts with sensor interfaces and precise collecting mechanical feedback signals [8], demonstrating substantial synergistic potential with the ultrasound technology across diverse application scenarios, making them ideal materials for flexible sensing and ultrasound energy harvesting devices. eGaInSn, leveraging its intrinsic properties, can effectively enhance interfacial electronegativity [10] and accelerate electron migration rates [19] under mechanical stress, thereby significantly boosting energy conversion efficiency [20,21]. yet their potential for non-contact operation remains untapped. Existing LM-based generators, like their solid counterparts, are constrained to contact-separation cycles, failing to leverage LM's inherent ability to undergo high-frequency microfluidic elastic deformation with minimal impedance properties uniquely suited to ultrasonic stimuli.

To address critical limitations in non-contact energy harvesting inefficient electromechanical conversion, weak force-electric coupling, and reliance on contact/inverters for DC output—we introduce a novel non-contact and flexible LM-based ultrasonic triboelectric DC generator for energy harvesting and sensing (LM-UHG) (Fig. 1a). The core of the LM-UHG is eGaInSn, which is engineered to perform two distinct yet complementary functions: (i) Ultrasonic-Actuated Dynamic Behavior: Under 40 kHz ultrasound excitation, the eGaInSn droplet undergoes intense forced vibration and deformation, effectively serving as an oscillating actuator. This macroscopic motion directly drives the periodic charging and discharging of the electrical double layer (EDL) at the interface with a copper electrode. Concurrently, ultrasound-induced Marangoni flow within the LM drastically enhances ion transport, collaboratively forming a robust "charge pump" that efficiently primes the initial triboelectric charges. (ii) Role of the Native Ga_2O_3 Layer in Stabilizing the Interface: The inherent surface oxide layer is pivotal for maintaining a stable polarization state within the EDL. Furthermore, it acts as an innate triboelectric material when interacting with the elastomer, while also stabilizing the interfacial potential via surface passivation and interactions with ambient species. These mechanisms work in concert to significantly enhance the overall output voltage.

The minimalist architecture of the LM-UHG capitalizes on the intrinsic material advantages to achieve breakthrough electromechanical performance. Upon ultrasonic excitation (40 kHz, 30 W, 50 mm transducer diameter), the device delivers a remarkable load voltage of up to 2.5 kV in a two-electrode configuration. Notably, its single-electrode design achieves an exceptional open-circuit voltage as high as 6 kV, accompanied by short-circuit currents of 25 μA (single-electrode) and 688.8 μA (two-electrode). This high-output performance enables the direct driving of micro-electronic components without the need for inverter or physical contact. With less than 5% performance degradation over 7 days—attributed to LM's self-healing capability—it also serves as a self-powered ultrasonic/mechanical vibration sensor. This system achieves contactless mechanoelectrical transduction through innovative mechanisms, enabling simultaneous DC power generation and stress-sensitive signal acquisition in oxygen-containing environments, as evidenced by the energy flow framework in Fig. S1.

2. Results and discussion

2.1. Electrical signals generated by the eGaInSn under the action of ultrasonic mechanical stress

The LM employed in this study, eGaInSn (Fig. 1a), differs from conventional piezoelectric materials. A protective oxide layer (predominantly Ga_2O_3) spontaneously forms on its surface. This 0.7–3 nm thick oxide layer stabilizes the system by preventing further oxidation [22,23], yet its dynamic regeneration under mechanical stimuli (e.g., ultrasonic vibration) (Fig. 1b) are key to preventing electrical short-circuiting and ensuring stable interfacial contact (Fig. 1c i-ii) [24,25]. It remains liquid at room temperature with exceptional fluidity, conductivity, and unique interfacial dynamics under mechanical stress (Fig. 1d). The high energy conversion efficiency is critically governed by the liquid-phase adaptability of eGaInSn, with the dynamic oxide layer playing a key role in stabilizing this process.

The single-electrode configuration employed a copper electrode, with a 40 kHz ultrasonic transducer (diameter: 50 mm, power: 30 W) positioned at 5 mm above a beaker (base diameter: 50 mm) containing 10 g of eGaInSn (Fig. S1). Ultrasonic mechanical stress induces dynamic interfacial contact. The presence of the Ga_2O_3 layer stabilizes this contact. Specifically, the static state is shown in Fig. S1 i, where the electrode and the ultrasound are in a state of separation; starting the ultrasonic transducer causes local oscillation, resulting in friction charges as shown in Fig. S1 ii; as time reaches a threshold, the friction charges reach saturation as shown in Fig. S1 iii; turning off the ultrasonic transducer restores the overall static state as shown in Fig. S1 iv. A simplified charge separation mechanism based on the ultrasonic mechanical stress response is shown in Fig. 1e. From the perspective of vibration mode characteristics, the eGaInSn surface exhibits multimodal vibrations under ultrasonic excitation, with multiple vibration nodes (node) and antinodes (antinode) as shown in Fig. 1e i-ii [26]. The eGaInSn surface simultaneously contains upward and downward-moving antinode regions, as depicted in Fig. 1e iv. Regarding the electric potential cancellation mechanism, downward-moving antinode regions induce more charge separation at the eGaInSn surface (Fig. 1e iii). When the antinodes disappear, based on the intrinsic self-healing properties of eGaInSn, upward-moving antinode regions alter the charge separation density (Fig. 1e iv). Under the combined effects of the enormous surface tension and wrinkling of the LM surface, the electrical signal feedback of the eGaInSn under ultrasonic mechanical stress is significantly enhanced. Voltage measurement via a voltage-divider method revealed open-circuit voltages with peaks of 6 kV (Fig. S2a) [27], under a dual-electrode configuration, the output voltage reaches 2.5 kV when loaded with a 1 GΩ resistor (Fig. S2b), capable of directly powering 100 LEDs in series (Fig. 1f, Fig. 1g i, Supplementary Video S1), exceeding most reported nanogenerators (Table S1) [28–41], with concurrent current peaks of 25 μA (Fig. 1g ii), yielding a calculated peak power output of 7.62 mW/m^2 (Fig. S2c). When a high-efficiency output is required, ultrasound waves can be seamlessly coupled with a liquid-

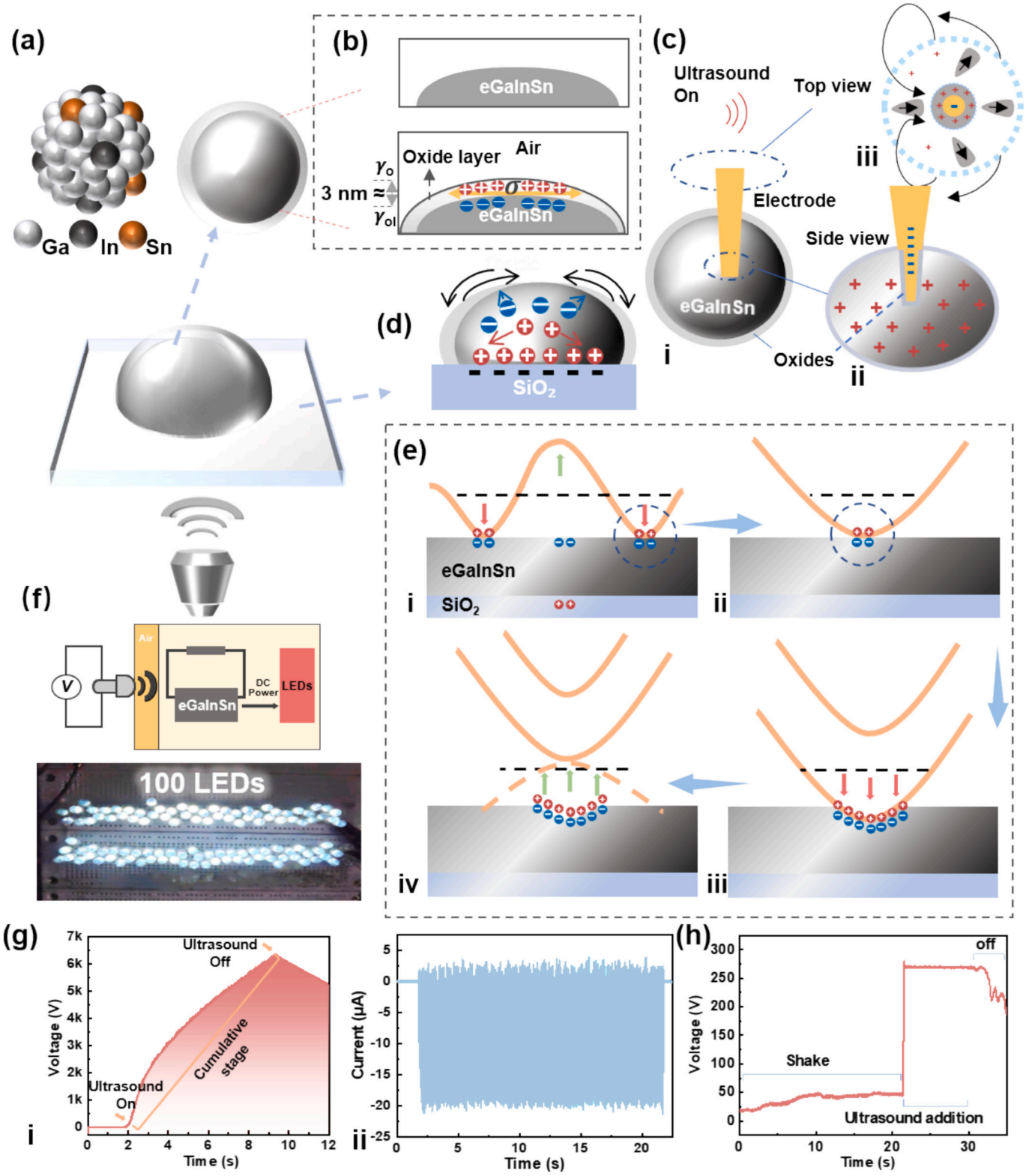

Fig. 1. (a) Schematic illustration of the LM-UHG. (b) Reduced and oxidized states of a LM droplet, native oxide of the eGaInSn and its two interfaces: the surface energy of the outward-facing interface, the interfacial energy of the inward facing interface, mechanical tension of the native oxide are denoted as γ_o, γ_{ol}, and σ, respectively. (c) i) Top view of the device, ii) Shielding effect of the oxidation barrier. iii) Simplified internal self-driving mechanism of the eGaInSn when subjected to ultrasonic mechanical stress. (d) Change of the charge in the eGaInSn droplet model under the influence of ultrasonic wave. (e) Simplified charge separation mechanism based on ultrasonic mechanical stress response. (f) Application circuit diagrams and LED lighting applications. (g) i) Voltage signal diagram, ii) Current signal diagram. (h) Realize monitoring of the surrounding vibration environment with zero power consumption, and the vibration energy can be seamlessly coupled with ultrasound, making it applicable to different application scenarios.

metal-based high-voltage DC generator, thereby enabling power amplification and facilitating intelligent, efficient on-demand energy supply in practical application scenarios (Fig. 1h).

The electrical signals originate from the interfacial material properties and ultrasonically driven dynamic charge separation [25]. Stress-induced formation of EDL between the eGaInSn and hybrid interfaces (silica beaker/electrode) creates charge inhomogeneity due to electronegativity disparity, prompting dynamic ionic migration [42,43]. Ultrasonic stress induces interfacial wrinkling, a process regulated by the oxide layer, which in turn stabilizes the distribution of the EDL (Fig. 1d). Concurrently, an ultrasound-activated Marangoni flow promotes interfacial charge reconfiguration to boost energy conversion kinetics (Fig. 1c iii) [44].

To elucidate the energy generation mechanism of LM-UHG, we developed an equivalent circuit model integrating three capacitive components ($C_{eGaInSn}$, C_{EDL1}, and C_{EDL2}), two impedance elements (the eGaInSn impedance R_G and load impedance R_L), and a voltage source V_P (the potential difference between "P" and mirror "S" is defined as V_P) (Fig. S2d). The V_P parameter was used to represent the synergistic relationships among key parameters including dielectric layer thickness, eGaInSn droplet ion concentration, and material composition. Given that the eGaInSn thickness exceeds that of both EDL by several orders in magnitude, according to the planar capacitor formula $C = \frac{\varepsilon S}{d}$ the capacitance is inversely proportional to the thickness d of the dielectric layer, that is, the capacitance of eGaInSn is much smaller than that of the EDL capacitor. In a series circuit, the total capacitance is dominated by the smallest capacitance. Consequently, the total equivalent capacitance of the system can be approximated by the $C_{eGaInSn}$ component. The energy conversion process manifests through eGaInSn droplet-electrode-dielectric interactions forming a closed-circuit system, where the V_P-gated charge transfer occurs via $C_{eGaInSn}$ and R_G to the external load R_L. The controlled adjustment of the ultrasonic enables precise modulation of interfacial capacitance ($C_{eGaInSn}$), gate voltage (V_P), and impedance characteristics (R_G), thereby establishing a programmable framework for optimizing LM-UHG with power output.

The device with simplified architecture exhibits reliable and versatile energy capture performance in high-efficiency regimes while maintaining functionally integrated compact system. Eliminating the need for a rectification circuit, thereby validating the potential for integrating nanogenerator-based devices into energy systems for compact, wireless, and implantable electronics. Additionally, the cyclic deformation of the eGaInSn under mechanical stress and its gravity-driven steady-state recovery ensure structural integrity and consistent electrical performance over an extended period. The oxide layer facilitates rapid and uniform stress transmission across the interface, which is essential for guaranteeing the long-term operational stability and consistent output efficiency of the device [45].

2.2. Material characterization and structural analysis

To verify the cooperative effect of the gas-solid-liquid type elastomer interface (G-S-L) in the LM-UHG, we systematically characterized eGaInSn, correlating its structural/chemical properties with the device's 6-kV V_{oc} and less than 5% performance degradation within 7 days.

2.2.1. Scanning electron microscopy (SEM)

The morphological evolution of eGaInSn under 40 kHz ultrasonic excitation was observed using SEM. Before ultrasonic treatment, the surface oxide layer of eGaInSn formed a smooth film on silica. After cumulative ultrasonic stress stimulation for 10 h (Fig. 2a), macroscopic wrinkles appeared, along with distinct Ga_2O_3 self-healing traces; high-magnification images revealed fine wrinkles. This enhanced roughness modulated the EDL at the surface driven by the Marangoni flow within eGaInSn: the multimodal eGaInSn vibration induced by ultrasonic waves combined with the elastic substrate deformation activated the "elastic body-mediated charge pump" (Fig. 1c iii, Supplementary Video S2), which was confirmed by in-situ video related to SEM (Supplementary Video S3).

2.2.2. Energy dispersive spectroscopy (EDS) analysis

EDS analysis confirmed the elemental homogeneity of eGaInSn, which is crucial for the sustained G-S-L type elastomer synergy (Fig. 2b). The uniform distribution of gallium, indium, and tin after ultrasonic treatment indicates that the LM phase remains intact under prolonged mechanical stress. The oscillating oxygen content reflects the dynamic redox of the native Ga_2O_3 layer: repeated rupture and regeneration regulate the thickness of the oxide, while the valence states of gallium, indium, and tin remain stable (verified by XPS). This self-healing behavior results in a frequency scanning performance decay of less than 5% within 7 days.

2.2.3. X-ray diffraction (XRD)

X-ray diffraction excluded the crystal transformation in eGaInSn and confirmed the amorphous state of Ga_2O_3 (Fig. 2c). The characteristic peak of the eGaInSn ($2\theta = 34.5 \pm 0.1°$) did not shift, indicating adaptive recovery and elastic deformation under ultrasonic stress. The broad background signal (2θ = 25–50°) indicated that the native Ga_2O_3 layer was amorphous, and no crystalline peaks were detected. This amorphous structure reduced grain boundary scattering, facilitating EDL polarization and thus achieving efficient charge separation.

2.2.4. Infrared thermal imaging

Infrared thermal imaging quantified the interfacial heating at the silica-eGaInSn interface, a key factor for G-S-L type elastomer coupling (Fig. 2d). Before ultrasonic treatment, the interface temperature was uniform (22.8–23.1 °C); after 5 min of stimulation, a local hot spot reached 27.4 °C. This temperature rise was driven by ultrasonic micro-displacement (Supplementary Video S3). The hot spot amplified the electronegativity difference between silica and eGaInSn, enhancing G-S-L type elastomer chemomechanical coupling.

2.2.5. X-ray photoelectron spectroscopy (XPS)

XPS revealed that the charge separation mechanism of LM-UHG was different from the traditional triboelectric/piezoelectric process (Fig. 2f). The Ga 2p spectrum showed that the Ga^{3+} peak (Ga_2O_3, 1113 ± 0.2 eV) increased in intensity after ultrasonic treatment; the metal Ga peak (1111 ± 0.2 eV) correspondingly weakened. In contrast, the In 3d (438 ± 0.1 eV) and Sn 3d (479 ± 0.1 eV) spectra remained in the pure metallic state (no In_2O_3 or SnO_2 peaks), confirming selective Ga oxidation, a significant difference from solid-solid triboelectric systems [46].

2.2.6. Contact angle measurement

Contact angle measurement linked the dynamic changes of Ga_2O_3 to the wettability of the G-L interface (Fig. 2e). After 10 h of ultrasonic treatment, the non-uniformity of the oxide layer thickness increased the surface tension, reducing the contact angle of eGaInSn on silica by approximately 5° (from 130.2° to 125.4°). Due to the reduction in grain boundary scattering, the thinner amorphous Ga_2O_3 layer had higher conductivity than the thick polycrystalline layer, and the enhanced wettability optimized the propagation of ultrasonic waves at the G-L interface.

2.2.7. Work function evolution

Unlike its constituent metals (gallium melts at 29.8 °C, close to room temperature but prone to partial solidification; indium and tin are solid at ambient conditions and melt at 156.6 °C and 231.9 °C, respectively), eGaInSn remains liquid at room temperature. The work function (Φ = 4.30 ± 0.02 eV) of eGaInSn was measured by Kelvin probe force microscopy, which lies between that of pure Ga (4.10 eV), In (4.60 eV), and Sn (4.40 eV) (Fig. 2g i). This intrinsic fluidity of liquid metal enables conformal, self-adaptive contact under dynamic mechanical stress—a

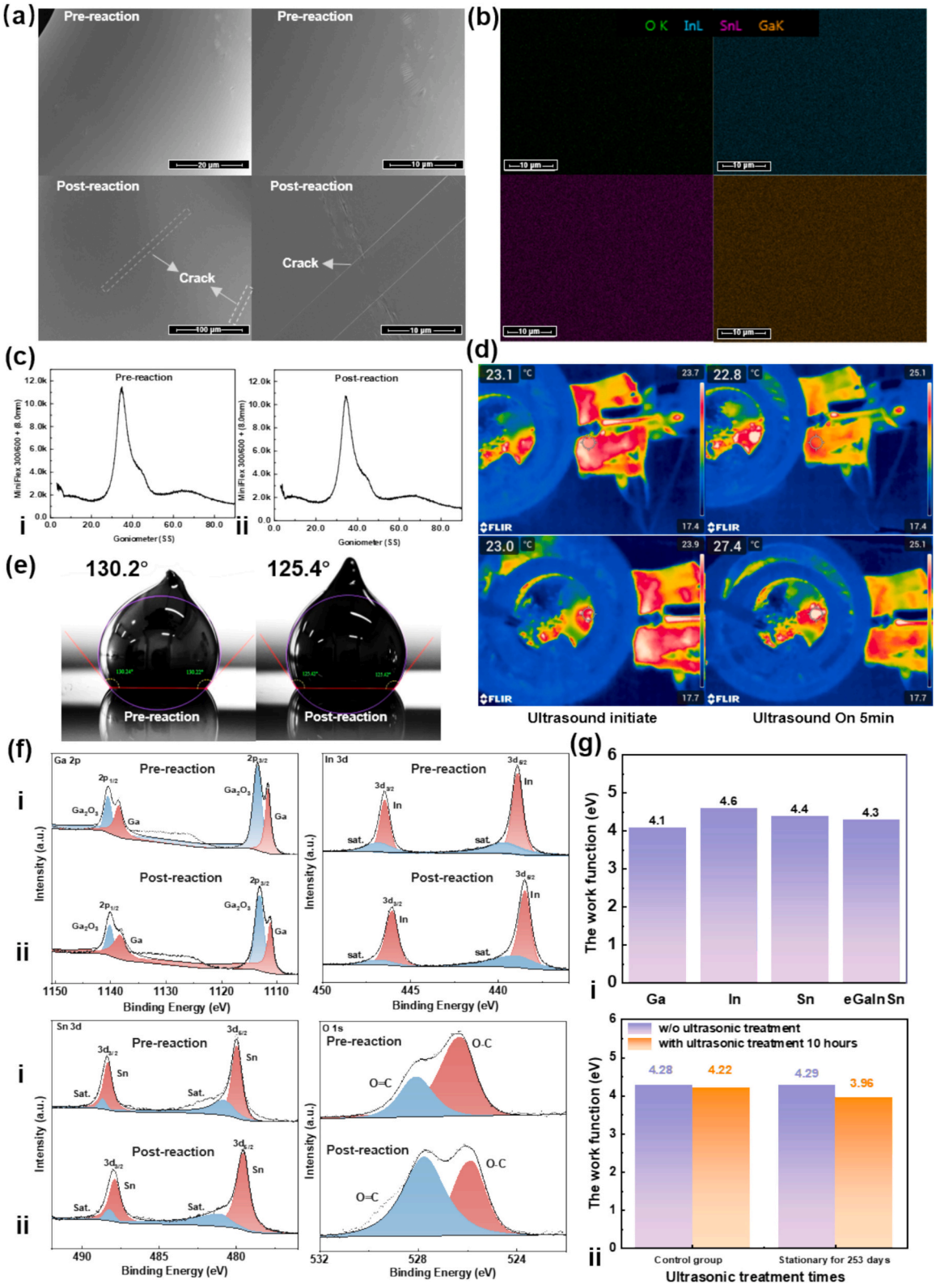

Fig. 2. (a) The surface morphology characteristics of the eGaInSn oxide layer under SEM are presented separately for those that have not undergone ultrasonic treatment and those that have accumulated 10 h of ultrasonic treatment. (b) The mapping of the distribution of Ga, In, and Sn elements in eGaInSn under EDS surface scanning results. (c) The XRD results of the eGaInSn surface oxide layer, presented separately for those that have not undergone ultrasonic treatment and those that have accumulated 10 h of ultrasonic treatment. (d) The infrared images of eGaInSn and the ultrasonic transducer under ultrasonic conditions. (e) The contact angles are presented separately for those that have not undergone ultrasonic treatment and those that have accumulated 10 h of ultrasonic treatment. (f) The changes of XPS before and after ultrasonic treatment are i) never subjected to ultrasonic treatment, and ii) accumulated 10 h after ultrasonic treatment. (g) The characterization results of the work functions of i) Ga, In, and Sn, and ii) the changes of the work functions after 253 days, presented separately for those that have not undergone ultrasonic treatment and those that have accumulated 10 h of ultrasonic treatment.

behavior inherently unattainable with rigid solid metals, which are prone to irreversible wear and unstable interfacial contact. The uniform, self-healing electrical contact thus achieved is not a mere convenience but an essential prerequisite: our proposed operating principle fundamentally relies on precisely such a dynamically reconfigurable liquid metal/electrode interface. Consequently, liquid metal serves as the indispensable enabler of this unique energy harvesting mechanism, rather than being a mere alternative conductive material.

After 253 days, the samples that had not undergone ultrasound and those that had received a cumulative total of 10 h of ultrasound showed changes in the work function as depicted in Fig. 2g ii. This surface activation enhances the interfacial electric field, and the combination of tunable work function and liquid-phase adaptability distinguishes eGaInSn from solid metal counterparts, broadening its application scope in flexible, non-contact energy harvesting scenarios.

These characterizations collectively paint a complete picture of the G-S-L type elastomer interface synergy: SEM and EDS confirmed the structural and elemental stability, XRD and XPS revealed the oxide-mediated charge separation, infrared imaging quantified the triboelectric heating effect, and contact angle/KPFM linked interface properties to electronic performance. This multi-dimensional validation highlights the unique advantage of LM-UHG: achieving high voltage and stable energy harvesting by leveraging the dynamic LM self-adaptive feature.

In addition, to quantitatively track the evolution of the Ga^0/Ga^{3+} ratio across multiple sonication cycles (1, 5, and 10 h) and thereby demonstrate the dynamic self-healing nature—rather than a simple

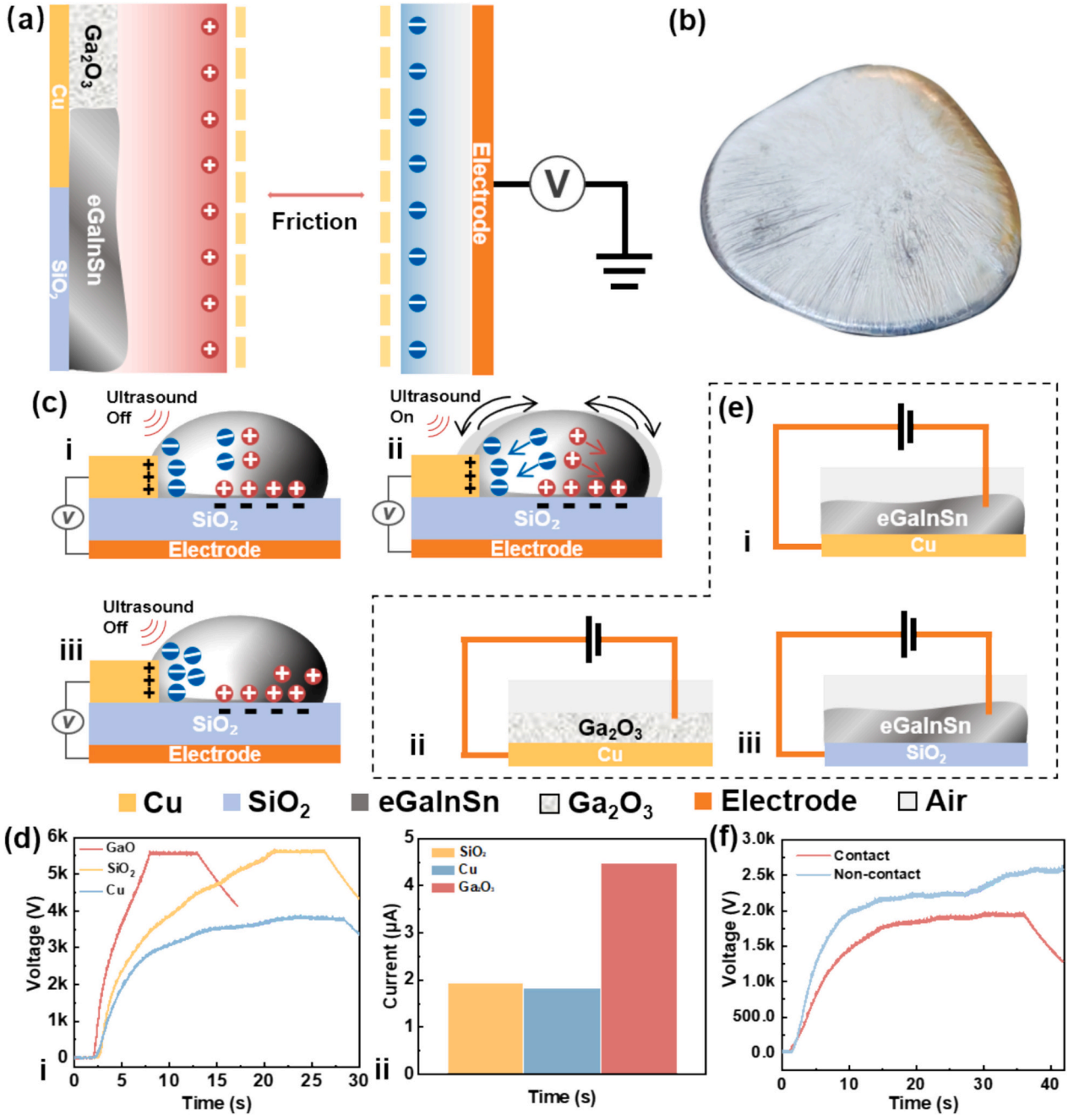

Fig. 3. (a) Electronegativity response diagram of different materials. (b) The properties of the oxide layer cause its surface to fold when subjected to mechanical stress. (c) Potential difference of droplet model in different states of ultrasonic coupling. (d) A brief diagram of the electrical signal changes of the three materials constituting the device under ultrasonic mechanical stress, i) voltage signal, ii) current signal. (e) Ultrasonic driven hybrid interface energy harvesting model. (f) Voltage of silicon dioxide and copper electrode under different conditions of contact and non-contact.

before-and-after comparison—XPS analysis was performed Fig. S3a. Corresponding SEM images are presented in Fig. S3b. Furthermore, to address the limitations of TEM characterization, we developed an innovative sample preparation protocol enabling direct measurement of the oxide layer's topographical changes via AFM before and after sonication. This approach establishes a more direct correlation between morphological evolution and functional properties, as shown in Fig. S3c. The voltage signals at different reaction time scales are shown in Fig. S4a.

2.3. Energy generation mechanisms and constitutive material responses under ultrasonic mechanical stress

This study establishes an ultrasonically driven hybrid interfacial energy harvesting framework that synergizes the liquid-phase elastomer adaptability and high energy density of the eGaInSn with ultrasound-mediated energy transduction across gas-solid (G-S), solid-liquid (S-L), and gas-liquid (G-L) interfaces (Fig. 3a and Fig. S4b) [47]. The system achieves multiphase interfacial synchronization for concurrent sensing and energy harvesting, distinct from conventional ultrasonic energy transfer paradigms, through the oxide-enabled interfacial charge polarization and ultrasonically induced microscale displacement impacts at the heterogeneous boundaries.

Under the ultrasonic mechanical stress, the interfacial interactions between the eGaInSn and heterogeneous boundaries significantly modulate energy harvesting efficiency. During the periodic microscale displacement impacts at the solid-liquid interface, the localized high-pressure and high-temperature zones form on the silica surface, intensifying the interfacial triboelectric effects [48,49]. As the silica beaker vibration under the stress excitation induces multiple ripple effects, the disparity in mechanical wave propagation rates between the silica and eGaInSn combined with the material-specific electronegativity responses synergistically promotes the interfacial charge separation.

At the G-S interface, the feedback vibration enhances the charge separation between gas, electrode, and beaker boundaries by altering the initial charge states and gas particle dynamics. These changes perturb the ionic concentrations within the diffusion layer, optimizing the charge distribution and improving the energy conversion efficiency.

Herein, at the G-L interface, microscale displacement of the eGaInSn and its oxide layer characteristics induce surface wrinkling (Fig. 3b). These wrinkles dynamically modulate a specific surface area and trigger the charge redistribution, thereby enhancing the charge separation efficacy. Ultrasonic enhancement of the mass transfer and adsorption kinetics synergistically elevates the energy absorption efficiency [50]. Ultrasound simultaneously intensifies the silica surface chemical activity and eGaInSn oxide reactivity [51]. While the static eGaInSn on silica shows a negligible potential difference (Fig. 3c i), however, when the droplet undergoes unidirectional continuous motion under the ultrasound-induced mechanical stress, cation species within the fluid selectively accumulate at the advancing interface due to interfacial electrokinetic effects (Fig. S4c, d). This dynamic redistribution of the ionic charges disrupts the homogeneous surface charge equilibrium of the eGaInSn, thereby establishing a relative potential gradient along the droplet. Such potential difference initiates the directional electron migration within the bulk eGaInSn, generating a sustained charge transport pathway. The potential gradient persists throughout the droplet motion and approaches dynamic equilibrium as the droplet reaches the terminal region of the eGaInSn channel (Fig. 3c ii) [52,53]. When the ultrasonic wave stops working, the charge distribution returns to the steady state, the charge separation is shown in Fig. 3c iii.

Through the ultrasonically activated interactions across the G-S, solid-liquid, and G-L interfaces, the eGaInSn elastic achieves efficient mechanical energy harvesting. At the solid-liquid interface, the microscale displacement-induced charge separation dominates the energy conversion. The G-S interactions amplify the triboelectric effects via the air vibration-modulated initial charge states, while the G-L interfacial dynamics enhances energy efficiency through the optimized ion concentration kinetics in the diffusion layer. These coordinated mechanisms synergistically elevate the overall system energy harvesting capacity.

To elucidate the component-specific behaviors under the ultrasonic mechanical stress, this work conducted comparative electrical characterization on silica, copper, and gallium oxide (Ga_2O_3). As shown in Fig. 3d i, the Ga_2O_3-Cu pair exhibited the fastest voltage rise rate, reaching 6 kV within 10 s. The SiO_2-eGaInSn combination achieved its voltage plateau at 20 s, followed by the Cu-eGaInSn pair stabilizing at 3.5 kV after 28 s, the average current signal is shown in Fig. 3d ii. The ultrasonic-driven hybrid interface energy harvesting model is shown in Fig. 3e i-iii. Remarkably, non-contact configurations between the silica and copper electrodes maintained substantial electrical output air-breakdowns under the ultrasonic excitation: contact voltage (1.9 kV) vs. non-contact (2.6 kV), and contact current (5.1 μA) vs. non-contact (2.5 μA) (Fig. 3f, Fig. S5a). The charge signal is shown in Supplementary Fig. S5b. Furthermore, under the ultrasound-induced stress at microscale gaps, dynamic capillarity is triggered between the eGaInSn interface and electrodes. During this process, the eGaInSn becomes confined within the microcavity formed by the upper and lower electrodes and the interfacial meniscus, with its local curvature reaching maximum deformation. As demonstrated in Fig. S6a, upon reaching the maximum stretching state, the eGaInSn droplet adheres to the copper electrode tip via interfacial adhesion dynamics, forming a transient liquid bridge that spans the interelectrode space.

2.4. Energy conversion mechanism and performance modulation synergistically mediated by G-S-L type elastomer three-phase interfaces

The exceptional energy conversion capability of the LM-UHG stems from the hierarchical synergy of three core mechanisms, all rooted in the G-S-L three-phase interfaces. This framework sequentially triggers, amplifies, and optimizes ultrasonic energy conversion, with each experimental observation directly linked to the intrinsic material properties (elastomeric flexibility of eGaInSn, bifunctional Ga_2O_3 layer) and interfacial dynamics.

2.4.1. Elastomer-mediated "Charge Pump": Triggering initial energy conversion

The elastomer-like liquid flexibility of eGaInSn (electrical conductivity: ~3.4×10^6 S/m; Young's modulus: ~1–10 Pa [54]) enables the first critical step of LM-UHG—converting ultrasonic mechanical energy into interfacial charge separation via the "charge pump" mechanism. Ultrasonic longitudinal waves induce "fluid-elastomer synergistic vibration" (Supplementary Video S3), during which eGaInSn exhibits multimodal oscillation (constrained by the acoustic boundary conditions of the silica beaker) while the elastomer matrix deforms to generate controllable strain (Fig. 1e i–iv). This mechanical input drives two cascaded processes at the Cu/eGaInSn interface:

First, periodic compression-expansion of the EDL (Fig. S6b). Under ultrasonic stress, the compact layer of the EDL thins, and ions (Ga^{3+}, In^{3+}, Sn^{2+}) from the Ga_2O_3 layer are driven into the diffuse layer, increasing the interfacial charge density relative to static conditions. Second, the Marangoni effect of eGaInSn (Fig. 1c iii) synergistically enhances this EDL oscillation: ultrasonic stress generates a surface tension gradient, accelerating directional fluid flow to further regulate ion distribution within the EDL. This combined effect produces a unidirectional "charge flow"-electrons are continuously extracted from the Ga_2O_3 layer and collected by the Cu (copper) electrode, forming an initial current source.

Experimental validation confirms the irreplaceable role of the elastomer: (1) Freezing eGaInSn to a solid state at low temperature (eliminating liquid-phase flexibility) reduces its current signal to 77.34% of that in the liquid state (Fig. S7a, b), as rigid solids cannot sustain EDL oscillation. Removing the Ga_2O_3 layer reduces the peak scanning current from 1.922 mA (liquid state with oxide layer) to 0.926 mA (liquid state

without oxide layer), a 51% reduction (Fig. S7a, c); (2) Solid-state eGaInSn (with Ga_2O_3) only reaches 0.8835 mA (Fig. S7b); (3) In containers with the same base area, non-uniformly distributed eGaInSn (control group) exhibits superior voltage/current output compared to the uniformly distributed standard group. The non-uniform configuration achieves a maximum voltage of 3.1 kV and the fastest power rise rate (steepest increase at 30 W), while the uniform group reaches a maximum voltage of 150 V (also with the fastest rise at 30 W) directly linking strain magnitude to charge pump efficiency. Manual control of single Cu electrode contact further modulates this process: continuous contact maintains stable voltage output (Fig. S8a, b, Supplementary Video S2), while intermittent separation disrupts EDL reconstruction and reduces output—validating the capacitor-like charge storage capability of the EDL [55,56].

2.4.2. G-S-L type elastomer interfacial synergy: Optimizing performance modulation

Synergy at the G-S-L type elastomer interfaces enables precise modulation of energy conversion efficiency, with performance tuned via ultrasonic power, geometric parameters, and force direction—all directly linked to EDL dynamics [47].

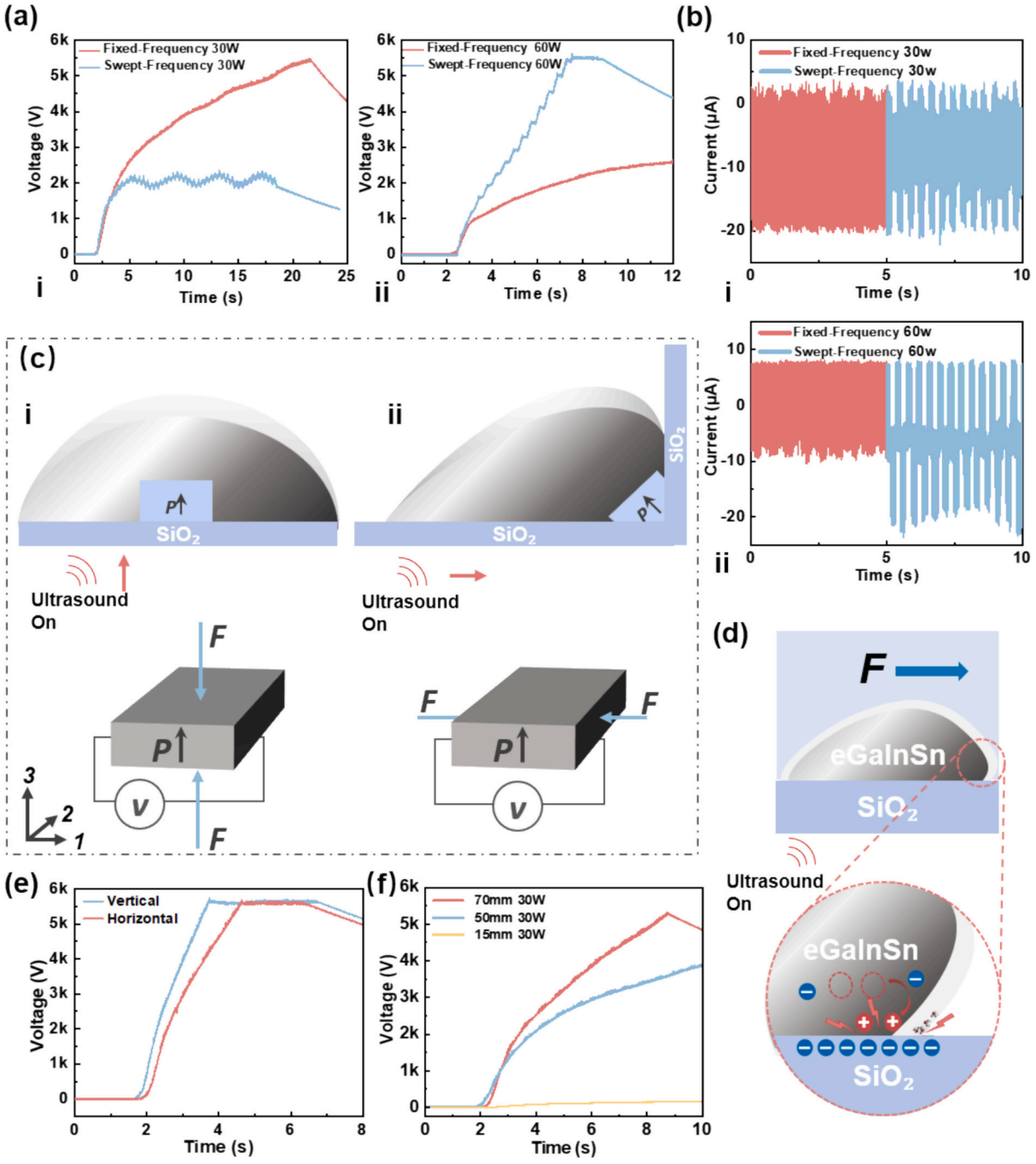

Fig. 4. (a) Comparison of voltage response to swept-frequency at i) 30 W and ii) 60 W power. (b) Comparison of current response to swept-frequency at i) 30 W and ii) 60 W power. (c) The stress of ultrasonic action at different angles is indicated, i) vertical direction ii) horizontal direction. (d) Charge separation at the boundary extension. (e) Feedback of sensing electrical signals from different ultrasonic stress directions. (f) Different bottom areas have a significant effect on the intensity of electrical signals.

2.4.2.1. Frequency-swept power dependence. The effect of frequency-swept operation on the LM-UHG's performance is critically governed by its power-dependent resonance matching with the system's natural frequency, which directly modulates the interfacial charge dynamics and overall resistance. This contrast unequivocally demonstrates the unique liquid-phase adaptability of our system, a feature absent in rigid TENGs [46].

At low power (30 W, below resonance), the frequency sweep acts as a disruptive perturbation. It hinders the stable formation of nascent EDL and interrupts the repair process of the native Ga_2O_3 layer. Consequently, the energy conversion efficiency is suppressed: the voltage output decreases by ~60% (2.2 kV vs. 5.5 kV, Fig. 4a i), the average current reduces by ~12% (7.66 μA vs. 8.74 μA, Fig. 4b i), and the interfacial resistance increases from ~3 MΩ to ~3.3 MΩ (Fig. S9a).

In stark contrast, at high power (60 W, at resonance), the frequency sweep synchronizes with the system's intrinsic dynamics. This synchronization enhances the coherent oscillation of the EDL, as a result, the interfacial synergy within the G-S-L type elastomer system is maximized, leading to a remarkable performance enhancement: the voltage increases by ~54% (5.6 kV vs. 2.6 kV, Fig. 4a ii), the current surges by ~56% (23.71 μA vs. 10.47 μA, Fig. 4b ii), and the resistance decreases. This power-dependent modulation, transitioning from inhibition to augmentation, provides direct evidence that resonance is key to activating the full potential of the three-phase interface.

2.4.2.2. Force direction-dependent sensing. Beyond energy harvesting, the LM-UHG exhibits an intrinsic capability for multimodal sensing, achieved through its unique response to directional mechanical stress. The underlying principle is that stress direction and magnitude dictate the spatial distribution of interfacial dynamics—namely EDL redistribution and Ga_2O_3 layer wrinkling—generating vector-selective electrical signals that directly correlate with the stimulus [57].

Under vertically incident ultrasound, a symmetric pressure gradient establishes a stable, reproducible pattern of central oxide adaptation and peripheral wrinkling (Fig. 4c i). The kinetics of this process, reflected in the voltage rise rate peaking at 3.7 ± 0.1 s (Fig. 4e), along with the resultant current magnitude (27 μA for a 50 mm beaker vs. 16 μA for a 70 mm beaker at 30 W, Fig. S10a i-ii), provides a direct metric for liquid level detection. A larger base area dissipates energy over a broader interface, reducing the current output.

Applying horizontal stress (Fig. 4c ii, Fig. 4d) or tilting the device to 45° breaks the symmetry, inducing lateral stretching-compression of the oxide layer, which nonetheless maintains interfacial stability throughout the deformation. This asymmetric deformation delays the voltage rise peak to 4.6 ± 0.1 s and generates spatially distinct current signals (Fig. 4e, Fig. S9b). Notably, when the electrode is positioned at the liquid surface edge—a region of maximal strain concentration—the current peak (37 μA) is significantly higher than at the center (22 μA, Fig. S10a iv, S10b ii). This geometric sensitivity is further amplified at higher liquid levels, where sharper current peaks (37 μA vs. 22 μA, Fig. S10b iii) are observed, confirming the capability to discern minute changes in surface height. The inclined configuration also promotes a pre-activation charge accumulation at the interface, manifesting as capacitor-like behavior prior to ultrasonic onset.

The exquisite sensitivity of the G-S-L type elastomer three-phase interface to the applied stress field enables the LM-UHG to transduce diverse mechanical stimuli—from impact direction to fluid geometry—into distinct electrical fingerprints, seamlessly integrating energy conversion with sophisticated self-powered sensing.

2.4.2.3. Geometric parameter modulation. The output of the LM-UHG is profoundly governed by geometric parameters that dictate the interfacial dynamics. Systematic investigations reveal that the container base area directly defining the solid-liquid (Cu-eGaInSn) contact area is a pivotal factor for EDL formation and overall charge capacity.

Expanding the base diameter from 50 mm to 70 mm enhances the voltage/current output by approximately 36%, whereas reducing it to 15 mm causes a drastic ~96% reduction (Fig. 4f, Fig. S11a). This monotonic trend unequivocally confirms that a larger interfacial area provides a more extensive platform for EDL oscillation and ion migration, thereby scaling up the total charge displaced by the "charge pump".

Beyond the absolute contact area, the spatial distribution of eGaInSn is equally critical. Non-uniform spreading of the LM (Fig. 5a i) generates localized strain fields that intensely amplify the EDL oscillation. This effect results in a phenomenal performance boost: the maximum voltage reaches 3.1 kV at 30 W, which is over 20 times greater than the 150 V achieved by a uniformly spread control group with the same mass (Fig. 5a ii). This striking contrast highlights that engineered micro-scale inhomogeneity can be a powerful strategy for maximizing the energy conversion efficiency of liquid-metal-based interfaces by focusing mechanical energy into active regions.

2.4.3. Thermo-triboelectric coupling: Enhancing interfacial dynamics

The energy conversion within the G-S-L type elastomer interface is further amplified by ultrasonically induced thermal effects, which create a synergistic thermo-triboelectric coupling. High-intensity ultrasound generates localized high-pressure and high-temperature zones at the interfaces (Fig. 2d, Supplementary Video S3), profoundly modulating the charge transfer kinetics.

The viscosity of eGaInSn decreases with rising temperature, leading to a linear increase in current output from 0 to 75 °C (Fig. 5e). This is attributed to accelerated ion migration within the EDL [48,49]. Furthermore, sustained ultrasonic excitation causes localized heat accumulation, potentially inducing microstructural fluctuations in eGaInSn and releasing latent heat. This thermal energy promotes interfacial reactivity and perturbs the EDL ion concentration gradients, thereby elevating the interfacial energy density.

The electrical output of the LM-UHG demonstrates a pronounced non-monotonic dependence on the input ultrasonic power, reaching a maximum at 30 W (Fig. 5b i-ii). This optimum arises from a fundamental competition between two power-dependent interfacial processes. At lower power levels, the mechanical stimulation provides sufficient interlude for the stable relaxation of the EDL, facilitating efficient charge separation. As the power exceeds this optimal point (>30 W), the accelerated interfacial dynamics severely shorten the available EDL relaxation time. Concurrently, the intense energy input promotes a rapid buildup of space charge, which establishes a counter-acting electric field that ultimately limits any further enhancement in output (Fig. 5c) [53].

The critical role of ultrasonic excitation in governing the interfacial charge transfer dynamics is further underscored by comparing current signals under different operational states. A marked difference is observed between the simple contact-separation of eGaInSn in the absence of ultrasound and the dynamic processes activated under both fixed-frequency and swept-frequency excitation (Fig. 5d).

The culmination of this optimized interfacial synergy at intermediate power levels is directly corroborated by the charging performance of a 47 μF capacitor. The charging rate reaches its peak at power levels ≥20 W and is sustained across higher powers (Fig. 5f), a trend fully consistent with the output characteristics of the device itself. Collectively, these results confirm that the ultrasonic power dictates the dynamic balance between charge generation and dissipation at the G-S-L type elastomer interface, with the performance maximum representing the optimal operational regime for the core energy conversion mechanism.

2.5. Stability: Sustained performance and reproducibility enabled by oxide-Interface synergy

Long-term stability is a key advantage of LM-UHGs over traditional TENGs, enabled by the dynamic self-healing of the Ga_2O_3 layer and environmental adaptability of the G-S-L type elastomer interface. To address concerns about the reproducibility of the reported high-

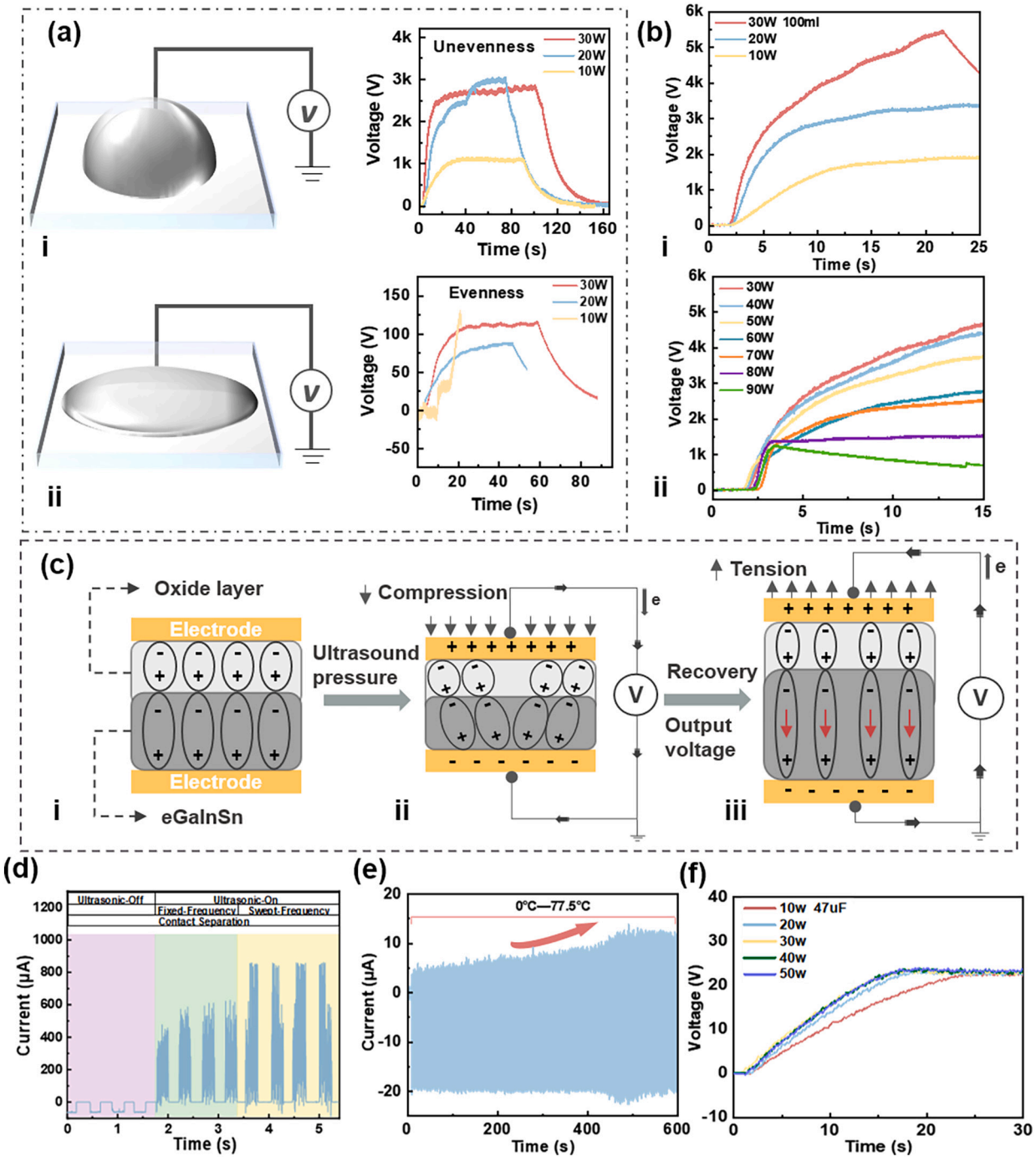

Fig. 5. (a) The impact of the liquid level shape on the electrical signal feedback. (b) The ultrasonic power dependence of the output voltage, showing maximum output at 30 W. Beyond this point, the signal drops, forming a normal distribution. (c) The energy collection mechanism is achieved by applying mechanical stress from ultrasound to the eGaInSn and its oxide layer for compression and stretching. (d) The difference in current signals between the contact and separation of eGaInSn without ultrasonic waves and that with fixed frequency and sweep frequency ultrasonic waves turned on. (e) Change of the current at 0–75 °C. (f) The rate at which a 47 μF capacitor is charged at different powers.

performance metrics, a 7-day systematic cyclic stability test was conducted using a standard two-electrode configuration. This configuration establishes a closed circuit with well-defined anode-cathode interfaces, eliminating errors from unstable contact resistance or stray charge accumulation; electrode spacing (1 mm) and material pairing (Cu/eGaInSn) were maintained constant throughout the test to ensure consistent current paths, minimizing variability from hardware configuration. Detailed stability characteristics and reproducibility validation are presented below, with all observations linked to the core electromechanical coupling mechanism.

Over the seven-day testing period under swept-frequency excitation, the device output demonstrated exceptional consistency. The average current was measured at 886.4 ± 49.4 μA (mean ± standard deviation), corresponding to a coefficient of variation (CV) of merely 5.57%. The performance on day 7 (888.2 μA) was virtually identical to the baseline established on day 1 (884.4 μA), showing a negligible deviation of +0.43% and confirming the absence of significant degradation. A transient fluctuation observed on day 6 (786.9 μA), approximately

11.2% below the mean, was conclusively linked to a drop in ambient humidity. The subsequent recovery of the output current on day 7, as humidity levels returned to baseline, underscores the reversible nature of this environmental response rather than an irreversible material failure (Fig. S12a, b). This resilience is a direct consequence of the non-contact operation mechanism and the regenerative Ga_2O_3 interface.

This significant improvement in electrical performance is directly attributed to the presence of the surface Ga_2O_3 layer. This layer not only effectively reduces the interfacial energy and inhibits excessive interface fluctuations, but its unique dynamic self-repairing ability can also maintain the integrity of the solid-liquid interface in real time, thereby ensuring the stability of the charge collection and transmission process. To rigorously address the requirement for performance reproducibility across multiple devices, we fabricated and characterized four independent devices ($n = 4$) under carefully controlled conditions. The results from all four devices consistently demonstrate that the presence of the surface oxide layer dramatically improves output stability. (Fig. S12c, d).

Pre- and post-test material characterization provides direct evidence for the proposed oxide-mediated self-healing process. XPS and EDS analyses performed before and after 10 h of continuous ultrasonic stress confirm the stability of the interfacial chemistry (Fig. 2b, f). While the oxygen content within the Ga_2O_3 layer exhibits minor fluctuations, the chemical states of the constituent elements—specifically, Ga^{3+} ($2p_{3/2}$ at 1111 eV), In^{3+} ($3d_{5/2}$ at 438 eV), and Sn^{2+} ($3d_{5/2}$ at 479 eV)—remain unchanged. This confirms that the interfacial processes are dominated by reversible redox-mediated regeneration, with no evidence of irreversible oxidation or compositional degradation.

To decouple intrinsic material degradation from environmental influences, output current was monitored daily under both fixed-frequency and swept-frequency excitation, while ambient conditions (temperature, humidity) were recorded concurrently. The results reveal two distinct operational paradigms:

In swept-frequency mode, the output exhibits excellent reproducibility and a predictable, reversible dependence on ambient humidity—a behavior fully consistent with the EDL modulation mechanism. Under high-humidity conditions (Days 1–2, 5, 7), the current remained stable between 872.6 and 934.1 μA. The transient current decrease of ~11% on the low-humidity Day 6 is attributed to a humidity-induced structural reorganization of the EDL, where a reduced water content thickens the compact layer, thereby slowing ion migration. The complete recovery of output on Day 7 confirms that this is a reversible physicochemical response, not a permanent degradation.

In fixed-frequency mode, which amplifies time-dependent material responses, a gradual, linear decrease in current was observed from Days 4 to 6, culminating in a value of 415.3 μA on Day 6. This trend is attributed to a combination of the reversible humidity effect and a slow, intrinsic interfacial fatigue at the eGaInSn-substrate interface under sustained static stress. Crucially, when humidity returned to high levels on Day 7, the current rebounded to 543.8 μA—a 30.9% increase from the previous day—confirming that the environmental component is fully reversible. The underlying intrinsic degradation proceeds at a quantifiable, predictable rate, providing reliability by avoiding catastrophic failure modes.

Notably, the observed humidity sensitivity is not merely an operational variable but an embodiment of the LM-UHG's integrated "energy harvesting-sensing" functionality. As the EDL is central to the energy conversion process, its inherent responsiveness to humidity simultaneously enables environmental monitoring. This dual character enhances the scientific value of the device while maintaining performance reproducibility. Under identical humidity conditions, the frequency-swept current deviates by less than 5%, confirming stable and consistent performance across cycles. Environmental fluctuations induce reversible output changes, while intrinsic degradation follows a predictable kinetic profile, collectively ensuring the reliability and reproducibility of the LM-UHG.

2.6. Applications of LM-UHG as a self-powered platform for integrated sensing and energy delivery

The hierarchical synergy within the G-S-L type elastomer interface unlocks a multifunctional platform that transcends conventional energy harvesters. This unique combination enables the LM-UHG to function as a core building block for self-powered systems capable of both perceiving environmental stimuli and delivering usable energy.

2.6.1. Ambient acoustic and vibration energy harvesting

The LM-UHG efficiently scavenges low-intensity mechanical energy from the environment. Under ultrasonic excitation (40 kHz, 30 W), the pronounced wrinkling at the G-L interface the effective contact area for triboelectrification (Fig. 3b). Coupled with the high-voltage output from the S-L EDL, the device generates distinct electrical signals in response to table tapping (15 V) and drumbeats (55 V) (Fig. 6a i, Fig. S11b), demonstrating its capability for harvesting broadband acoustic energy.

2.6.2. Multimodal sensing via interfacial responsiveness

The inherent sensitivity of the interfacial components enables sensing without additional functionalization.

Electrostatic Field Mapping: Charge polarization mediated by the native Ga_2O_3 layer (G-S interface) allows for non-contact detection. Using an electrostatic gun, the device records a rapid voltage rise (0.1 kV in 0.3 s) upon charge injection and an immediate drop upon release (Fig. 6a ii), showcasing potential for industrial electrostatic monitoring.

Humidity and Force Vector Detection: As established in stability tests, the G-L interface wrinkling is modulated by ambient humidity, enabling reversible humidity sensing. Furthermore, the vector-selective response of the S-L EDL to force direction—evidenced by distinct voltage rise kinetics for vertical (3.7 ± 0.1 s) versus horizontal stress (4.6 ± 0.1 s)—provides a mechanism for determining mechanical force orientation, relevant for structural health monitoring (Fig. 4e).

2.6.3. Conformal human-machine interaction glove

The material's inherent flexibility (Young's modulus: 1–10 Pa [54]) allows for seamless integration into wearables. A sensing glove was fabricated by printing eGaInSn onto conformal polyimide tape. The S-L interface's exquisite sensitivity to micro-deformation enables the discrimination of various hand actions based on their unique voltage signatures (harp peaks for typing ~20 V, sustained signals for mouse usage ~15 V), establishing a direct pathway for intuitive human-machine interfaces (Fig. 6b).

2.6.4. A 1-to-N ultrasonic broadcast Array for IoT power supply

To address the "power desert" challenge in distributed IoT networks, we developed a scalable ultrasonic energy broadcast system. A single transmitter (40 kHz, 50 W) powers multiple LM-UHGs of different geometries. The current output scales with the container base area, with the largest unit (200 mm diameter) reaching 5.831 mA under swept-frequency excitation (Fig. 6c). When connected in parallel, the array produced a transient current spike of ~25 mA. This aggregated output, significantly exceeding the simple sum of individual steady-state peaks, highlights the system's ability to harness energy from a common source across multiple nodes efficiently. The omnidirectional energy reception of the G-L interface and the stable interconnection provided by the G-S oxide layer are key to this scalable, broadcast-mode energy delivery paradigm.

In summary, the LM-UHG platform leverages its multi-interface synergy to achieve a triple integrated capability: non-contact energy harvesting, multimodal sensing, and scalable power delivery. This functionality, unattainable by traditional single-interface devices, provides a core technology for next-generation self-powered systems in industrial monitoring, wearable electronics, and the expansive IoT (Fig. S13).

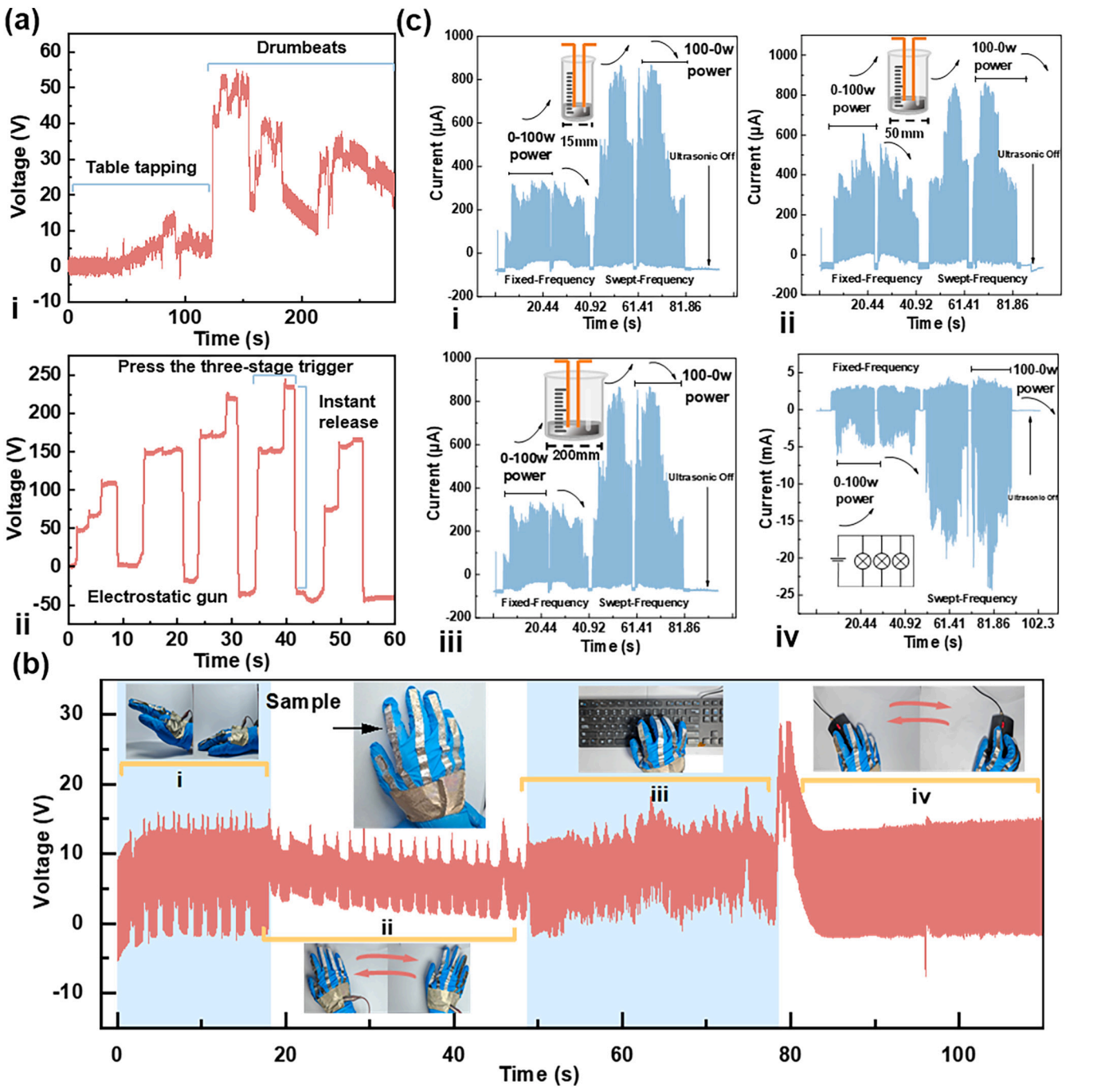

Fig. 6. (a) LM-UHG collects energy from i) sound and ii) static electricity in the surrounding environment through sensing. (b) The ultrasonic energy harvesting sensing glove made of LM-UHG material can precisely and continuously collect common action signals, and distinguish the signals corresponding to four different gestures. (c) The bottom diameters are i) 15 mm, ii) 50 mm, iii) 200 mm, and iv) three devices in parallel. Current signals of LM-UHG under fixed frequency and sweep frequency conditions with ultrasonic power cycled from 0 to 100 W.

3. Methods

3.1. The preparation of room temperature multiphase eGaInSn metals

The Ga, In, Sn were purchased from Shanghai Aladdin Company, while the Ga, In and Sn metal particles were mixed in a mass ratio of 67:20.5:12.5 to obtain the $Ga_{67}In_{20.5}Sn_{12.5}$ alloys (with a melting point of 10.5 °C).

3.2. Preparation of LM-UHG

eGaInSn weighing 10 g was loaded into a silica beaker and charge collection was carried out with Cu as the output end in a unipolar mode.

3.3. Measurements and characterizations

The SEM tests were conducted using a Zeiss Sigma 300 instrument. Energy Spectrum Scanning (EDS) tests were performed with an Oxford Xplore30 system. The X-ray diffraction (XRD) pattern was obtained with the Smart Lab SE Xray diffractometer (Cu Kα1, λ = 1.54056 A, 40 kV, 15

mA) in the 2θ range of 10° to 90°. X-ray Photoelectron Spectroscopy (XPS) tests were carried out using a Thermo Fisher Sci-entific K-Alpha+ instrument. The V_{oc}, I_{sc} and Q_{sc} of LM-UHG were characterized using an electrometer (Keithley 6514). The ultrasonic excitation was provided by an industrial system (Ultrasonic Generator: THDT3, Shenzhen Taiheda Technology Co., Ltd.). A piezoelectric transducer with a nominal resonant frequency of 40 kHz was used. All experiments reported in this work were conducted at this fixed frequency of 40 kHz, with the input power varied from 0 to 100 W. Regarding handling precautions, due to its low melting point, the eGaInSn alloy should be stored and handled above ~15 °C to prevent partial solidification and ensure consistent fluidic properties during experiments. All experiments were therefore conducted in a climate-controlled laboratory maintained at 22 ± 3 °C, with relative humidity strictly regulated to ≤35%. This stringent environmental control ensured both the sustained liquid integrity of the eGaInSn alloy and the high reproducibility and reliability of all electrical measurements throughout the entire study.

4. Results and discussion

This study addresses three critical limitations in conventional nanomechanical generators: (i) interfacial contact constraints, requiring physical interface interaction for energy harvesting, (ii) AC output necessitating rectification, and (iii) absence of integrated sensing-energy conversion architectures. We propose a non-contact hybrid energy-sensory DC generator based on the eGaInSn that eliminates reliance on inverter. This integrated architecture achieves DC output while maintaining compact dimensions suitable for miniaturized applications. Leveraging the exceptional fluidity, and high electrical conductivity of the eGaInSn, the system achieves concurrent sensory detection, hybrid energy harvesting, and efficient DC power generation under the ultrasonically induced non-contact mechanical stress. By incorporating multi-modal energy capture mechanisms, this generator achieves full-process energy conversion from morphological micro-displacements to stable high-voltage DC outputs. Its self-sustaining sensing capability enables continuous detection of ambient mechanical stimuli with zero power consumption while accumulating low-frequency acoustic energy. The on demand, seamless ultrasonic coupling amplifies power output to meet specific operational requirements. Our device delivers high-voltage DC output without requiring any external rectification circuit, enabled by a minimalist architecture that uniquely integrates non-contact operation, intrinsic DC generation, and sensing capabilities within a single platform. Through systematic analysis of its working mechanism and key material properties, we have developed an equivalent circuit model that accurately captures our experimental observations. In contrast to conventional contact-mode harvesters, our system harnesses four synergistic effects: charge separation, electrical double layer (EDL) modulation, dynamic surface area variation, and redox reactions. The liquid metal interface provides three distinct advantages: durable and conformal contact that eliminates wear-induced degradation; autonomous self-healing that ensures long-term stability; and broadband low-frequency tolerance that enables efficient operation under irregular excitations where conventional harvesters fail.

By shifting the paradigm of nanogenerator research from single-mode contact systems toward adaptive, multi-material platforms, this work establishes a new class of energy harvesting technology. The resulting platform—combining non-contact operation, inherent DC output, sensing capability, flexibility, and self-healing—is exceptionally well-suited for demanding applications. Its battery-free design inherently reduces maintenance costs and mitigates replacement risks, making it particularly attractive for implantable medical devices, brain-machine interfaces, and distributed sensor networks where reliability, longevity, and minimal intervention are critical.

CRediT authorship contribution statement

Tao Lin: Writing – review & editing, Writing – original draft, Visualization, Validation, Methodology, Investigation, Formal analysis, Data curation, Conceptualization. **Jiangtao Guo:** Writing – review & editing, Supervision, Conceptualization. **Qingju Liu:** Resources. **Zhigang Chen:** Investigation. **Yong Zhang:** Writing – review & editing, Supervision. **Wen Yang:** Resources. **Jun Wang:** Visualization. **Peizhi Yang:** Writing – review & editing, Supervision, Resources, Funding acquisition. **Liangfei Duan:** Writing – review & editing, Supervision, Funding acquisition, Conceptualization.

Funding

Yunnan Provincial Science and Technology Project at Southwest United Graduate School (202302A0370009).

The National Natural Science Foundation of China Projects (62465019).

Yunnan Province University Service Key Industry Science and Technology Projects (FWCY-ZNT2024008).

Yunnan Revitalization Talent Support Program; Spring City Plan: The High-level Talent Promotion and Training Project of Kunming (2022SCP005).

Yunnan Industrial Technology Innovation Reserve Talent Project (202105AD160056).

Reserve Talents Project for Youth and Middle-Aged Academic and Technical Leaders of Yunnan Province (202205AC160032).

Yunnan Fundamental Research Projects (202301AU070142, 202401AT070306, 202501AT070011, 202501AT070010).

The PhD Starting Fund program of Yunnan Normal University (2021ZB005, 01100205020503225).

Wisdom Yunnan Project (202403AM140035).

Project for Building a Science and Technology Innovation Center Facing South Asia and Southeast Asia (202403AP140015).

Authors thank the Electron Microscopy Center, the Advanced Analysis and Measurement Center of Yunnan University for the sample testing service.

Declaration of competing interest

The authors declare the following financial interests/personal relationships which may be considered as potential competing interests: Peizhi Yang reports financial support was provided by Yunnan Normal University. If there are other authors, they declare that they have no known competing financial interests or personal relationships that could have appeared to influence the work reported in this paper.

Appendix A. Supplementary data

Supplementary data to this article can be found online at https://doi.org/10.1016/j.cej.2026.175078.

Data availability

Data will be made available on request.

References

[1] H. Mei, Embracing informationization 3.0—an era of computing intelligence, SCIENCE CHINA Inf. Sci. 61 (2017) 010001, https://doi.org/10.1007/s11432-017-9299-1.

[2] S.A. Cummer, J. Christensen, A. Alù, Controlling sound with acoustic metamaterials, Nat. Rev. Mater. 1 (2016) 1–13, https://doi.org/10.1038/natrevmats.2016.1.

[3] W. Wei, Y. Wang, Z. Wang, X. Duan, Microscale acoustic streaming for biomedical and bioanalytical applications, TrAC Trends Anal. Chem. 160 (2023) 116958, https://doi.org/10.1016/j.trac.2023.116958.

[4] L. Zhang, et al., A conformable phased-array ultrasound patch for bladder volume monitoring, nature Electronics 7 (2024) 77–90, https://doi.org/10.1038/s41928-023-01068-x.

[5] S. Zhou, et al., Recent advances in TENGs collecting acoustic energy: from low-frequency sound to ultrasound, Nano Energy 129 (2024) 109951, https://doi.org/10.1016/j.nanoen.2024.109951.

[6] T. Yang, et al., Textured $CsPbI_3$ nanorods composite fibers for stable high output piezoelectric energy harvester, eScience 4 (2024) 100273, https://doi.org/10.1016/j.esci.2024.100273.

[7] S. Chen, J. Liu, Liquid metal enabled unconventional heat and flow transfer, Energy Sustain Energy Environ. (2019), https://doi.org/10.30919/esee8c318.

[8] S.K. Karan, et al., Magnetic field and ultrasound induced simultaneous wireless energy harvesting, Energy Environ. Sci. 17 (2024) 2129–2144, https://doi.org/10.1039/D3EE03889K.

[9] J. Guo, et al., Multiphase soft metal enabled high-performance fabric-based wearable energy harvesting, Nano Energy 131 (2024) 110305, https://doi.org/10.1016/j.nanoen.2024.110305.

[10] J. Guo, et al., Flexible triboelectric nanogenerator arrays for energy harvesting and direct current output via solid-liquid-gas interfaces involving liquid metals, Adv. Funct. Mater. (2025) e10233, https://doi.org/10.1002/adfm.202510233.

[11] H. Xiang, L. Peng, Q. Yang, Z.L. Wang, X. Cao, Triboelectric nanogenerator for high-entropy energy, self-powered sensors, and popular education, Sci. Adv. 10 (2024) eads2291, https://doi.org/10.1126/sciadv.ads2291.

[12] R. Liu, et al., Multifunctional smart fabrics with integration of self-cleaning, energy harvesting, and thermal management properties, ACS Nano 18 (2024) 31085–31097, https://doi.org/10.1021/acsnano.4c08324.

[13] K. Xia, M. Yu, Highly robust and efficient metal-free water cup solid–liquid triboelectric nanogenerator for water wave energy harvesting and ethanol detection, Chem. Eng. J. 503 (2025) 157938, https://doi.org/10.1016/j.cej.2024.157938.

[14] K. Xia, M. Yu, Y. Luo, Y. Ding, All-foam intrinsic triboelectric static and dynamic pressure sensor with a standardized DC/AC measurement method for industrial robots, Nano Energy 139 (2025) 110953, https://doi.org/10.1016/j.nanoen.2025.110953.

[15] K. Xia, Y. Hao, P. Luo, Y. Zhang, J. Guo, Z. Zhu, A faraday cage-inspired triboelectric nanogenerator enabled by alloy powder architecture for self-powered ocean sensing, Energy Environ. Mater. 8 (2025) e70040, https://doi.org/10.1002/eem2.70040.

[16] K. Xia, Z. Xu, Double-piezoelectric-layer-enhanced triboelectric nanogenerator for bio-mechanical energy harvesting and hot airflow monitoring, Smart Mater. Struct. 29 (2020) 095016, https://doi.org/10.1088/1361-665X/aba48d.

[17] Y. Dai, et al., Liquid metal droplets bouncing higher on thicker water layer, Nat. Commun. 14 (2023) 3532, https://doi.org/10.1038/s41467-023-39348-x.

[18] S. Chen, H.-Z. Wang, R.-Q. Zhao, W. Rao, J. Liu, Liquid metal composites, Matter 2 (2020) 1446–1480, https://doi.org/10.1016/j.matt.2020.03.016.

[19] C. Dong, et al., High-efficiency super-elastic liquid metal based triboelectric fibers and textiles, Nat. Commun. 11 (2020) 3537, https://doi.org/10.1038/s41467-020-17345-8.

[20] J. Fu, G. Xu, H. Wu, C. Li, Y. Zi, Liquid-interfaces-based triboelectric nanogenerator: an emerging power generation method from liquid-energy nexus, Adv. Energy Sustainability Res. 3 (2022) 2200051, https://doi.org/10.1002/aesr.202200051.

[21] B. Xu, et al., Liquid metal-based triboelectric nanogenerators for energy harvesting and emerging applications, Nano Energy 120 (2024) 109107, https://doi.org/10.1016/j.nanoen.2023.109107.

[22] L. Cademartiri, et al., Electrical resistance of AgTS –S(CH2) n −1 CH3 // Ga_2O_3 /EGaIn tunneling junctions, J. Phys. Chem. C 116 (2012) 10848–10860, https://doi.org/10.1021/jp212501s.

[23] J. Cutinho, et al., Autonomous thermal-oxidative composition inversion and texture tuning of liquid metal surfaces, ACS Nano 12 (2018) 4744–4753, https://doi.org/10.1021/acsnano.8b01438.

[24] W. Jung, et al., Giant decrease in interfacial energy of liquid metals by native oxides, Adv. Mater. (2024) 2406783, https://doi.org/10.1002/adma.202406783.

[25] D. Wang, X. Wang, W. Rao, Precise regulation of ga-based liquid metal oxidation, Acc. Mater. Res. 2 (2021) 1093–1103, https://doi.org/10.1021/accountsmr.1c00173.

[26] Y. Chung, et al., Gigantic triboelectric power generation overcoming acoustic energy barrier using metal-liquid coupling, Joule 8 (2024) 2681–2695, https://doi.org/10.1016/j.joule.2024.06.016.

[27] J. Dong, et al., A bio-inspired total current nanogenerator, Energy Environ. Sci. 16 (2023) 1071–1081, https://doi.org/10.1039/D2EE02621J.

[28] P. Zhang, W. Zhang, L. Deng, H. Zhang, A triboelectric nanogenerator based on temperature-stable high dielectric BaTiO3-based ceramic powder for energy harvesting, Nano Energy 87 (2021) 106176, https://doi.org/10.1016/j.nanoen.2021.106176.

[29] T.-T. Xu, S. Cheng, L.-Z. Jin, K. Zhang, T. Zeng, High-temperature flexural strength of SiC ceramics prepared by additive manufacturing, Int. J. Appl. Ceram. Technol. 17 (2020) 438–448, https://doi.org/10.1111/ijac.13454.

[30] S. Lin, L. Xu, A. Chi Wang, Z.L. Wang, Quantifying electron-transfer in liquid-solid contact electrification and the formation of electric double-layer, Nat. Commun. 11 (2020) 399, https://doi.org/10.1038/s41467-019-14278-9.

[31] Z.H. Loh, G. Doumy, C. Arnold, Observation of the fastest chemical processes in the radiolysis of water, Science 367 (2020) 179–182, https://doi.org/10.1126/science.aaz4740.

[32] Y.H. Wang, S. Zheng, W.M. Yang, In situ raman spectroscopy reveals the structure and dissociation of interfacial water, Nature 600 (2021) 81–85, https://doi.org/10.1038/s41586-021-04068-z.

[33] L. Sun, Z. Wang, C. Li, Probing contact electrification between gas and solid surface, Nanoenergy Adv. 3 (2023) 1–11, https://doi.org/10.3390/nanoenergyadv3010001.

[34] L. Wang, et al., Harvesting energy from high-frequency impinging water droplets by a droplet-based electricity generator, EcoMat 3 (2021) e12116, https://doi.org/10.1002/eom2.12116.

[35] J.H. Lee, S. Kim, T.Y. Kim, U. Khan, S.-W. Kim, Water droplet-driven triboelectric nanogenerator with superhydrophobic surfaces, Nano Energy 58 (2019) 579–584, https://doi.org/10.1016/j.nanoen.2019.01.078.

[36] Y. Chen, et al., Interfacial laser-induced graphene enabling high-performance liquid−solid triboelectric nanogenerator, Adv. Mater. 33 (2021) 2104290, https://doi.org/10.1002/adma.202104290.

[37] W. Xu, et al., A droplet-based electricity generator with high instantaneous power density, Nature 578 (2020) 392–396, https://doi.org/10.1038/s41586-020-1985-6.

[38] Z. Lin, G. Cheng, S. Lee, K.C. Pradel, Z.L. Wang, Harvesting water drop energy by a sequential contact-electrification and electrostatic-induction process, Adv. Mater. 26 (2014) 4690–4696, https://doi.org/10.1002/adma.201400373.

[39] J. Dong, et al., A high voltage direct current droplet-based electricity generator inspired by thunderbolts, Nano Energy 90 (2021) 106567, https://doi.org/10.1016/j.nanoen.2021.106567.

[40] X. Wei, et al., All-weather droplet-based triboelectric nanogenerator for wave energy harvesting, ACS Nano 15 (2021) 13200–13208, https://doi.org/10.1021/acsnano.1c02790.

[41] Q. Zhang, et al., An amphiphobic hydraulic triboelectric nanogenerator for a self-cleaning and self-charging power system, Adv. Funct. Mater. 28 (2018) 1803117, https://doi.org/10.1002/adfm.201803117.

[42] X. Li, R. Li, S. Li, Z.L. Wang, D. Wei, Triboiontronics with temporal control of electrical double layer formation, Nat. Commun. 15 (2024) 6182, https://doi.org/10.1038/s41467-024-50518-3.

[43] M.F. Wang, M.J. Jin, X.J. Jin, S.G. Zuo, Modeling of movement of liquid metal droplets driven by an electric field, Phys. Chem. Chem. Phys. 19 (2017) 18505–18513, https://doi.org/10.1039/C7CP02798B.

[44] H. Ren, et al., Light-controlled versatile manipulation of liquid metal droplets: a gateway to future liquid robots, Mater. Horiz. 8 (2021) 3063–3071, https://doi.org/10.1039/D1MH00647A.

[45] J. Liu, et al., Giant piezoelectric output and stability enhancement in piezopolymer composites with liquid metal nanofillers, Adv. Sci. 10 (2023) 2304096, https://doi.org/10.1002/advs.202304096.

[46] X. Liu, et al., Triboelectric nanogenerators exhibiting ultrahigh charge density and energy density, Energy Environ. Sci. 17 (2024) 3819–3831, https://doi.org/10.1039/D4EE00895B.

[47] X. Ye, Z. Zheng, J.G. Werner, J.W. Boley, Mechanically rupturing liquid metal oxide induces electrochemical energy, Adv. Funct. Mater. 34 (2024) 2309177, https://doi.org/10.1002/adfm.202309177.

[48] H. Wang, et al., Phase transition science and engineering of gallium-based liquid metal, Matter 5 (2022) 2054–2085, https://doi.org/10.1016/j.matt.2022.05.031.

[49] H. Wang, et al., Multi-stimulus perception and visualization by an intelligent liquid metal-elastomer architecture, Sci. Adv. 10 (2024) eadp5215, https://doi.org/10.1126/sciadv.adp5215.

[50] D. Hu, S. Liu, L. Qi, J. Liang, G. Zhang, A critical review on ultrasound-assisted adsorption and desorption technology: mechanisms, influencing factors, applications, and prospects, J. Environ. Chem. Eng. 12 (2024) 114307, https://doi.org/10.1016/j.jece.2024.114307.

[51] J. Wu, N. Qin, D. Bao, Effective enhancement of piezocatalytic activity of $BaTiO_3$ nanowires under ultrasonic vibration, Nano Energy 45 (2018) 44–51, https://doi.org/10.1016/j.nanoen.2017.12.034.

[52] S.S. Kwak, et al., Triboelectrification-induced large electric power generation from a single moving droplet on graphene/polytetrafluoroethylene, ACS Nano 10 (2016) 7297–7302, https://doi.org/10.1021/acsnano.6b03032.

[53] V. Vallem, et al., A soft variable-area electrical-double-layer energy harvester, Adv. Mater. 33 (2021) 2103142, https://doi.org/10.1002/adma.202103142.

[54] R.M. Pallares, X. Su, S.H. Lim, N.T.K. Thanh, Fine-tuning of gold nanorod dimensions and plasmonic properties using the Hofmeister effects, J. Mater. Chem. C 4 (2016) 53–61, https://doi.org/10.1039/C5TC02426A.

[55] Y. Liang, J. Gao, Q. Wang, N. Lu, Y. Zhang, X. Zhu, Self-healing micro-supercapacitor based on robust liquid metal-CNT-PEDOT:PSS film for wireless powering of integrated strain sensor, Small Methods (2024) 2401581, https://doi.org/10.1002/smtd.202401581.

[56] B.E. Conway, W.G. Pell, T.-C. Liu, Diagnostic analyses for mechanisms of self-discharge of electrochemical capacitors and batteries, J. Power Sources 65 (1997) 53–59, https://doi.org/10.1016/S0378-7753(97)02468-3.

[57] Y. Zhang, et al., Construction of liquid metal-based soft microfluidic sensors via soft lithography, J. Nanobiotechnol. 20 (2022) 246, https://doi.org/10.1186/s12951-022-01471-0.